Petroleum Science 21 (2024) 1354–1368

Contents lists available at ScienceDirect

Petroleum Science

journal homepage: www.keaipublishing.com/en/journals/petroleum-science

Original Paper

Inter-stage performance and energy characteristics analysis of electric submersible pump based on entropy production theory

Hui Wang [a], Yang Yang [a, b, e, *], Bin Xi [a], Wei-Dong Shi [c], Chuan Wang [a], Lei-Lei Ji [d], Xiang-Yu Song [e], Zhao-Ming He [f]

[a] College of Hydraulic Science and Engineering, Yangzhou University, Yangzhou, 225009, Jiangsu, China
[b] College of Electrical and Mechanical Engineering, Nanchang Institute of Technology, Nanchang, 330044, Jiangxi, China
[c] College of Mechanical Engineering, Nantong University, Nantong, 226019, Jiangsu, China
[d] National Research Center of Pumps, Jiangsu University, Zhenjiang, 212013, Jiangsu, China
[e] Zhejiang Zhenxing Petrochemical Machinery Co., Ltd., Ruian, 325204, Zhejiang, China
[f] Department of Mechanical Engineering of Texas Tech University, Lubbock, 79411, TX, USA

ARTICLE INFO

Article history:
Received 27 April 2023
Received in revised form
2 August 2023
Accepted 31 October 2023
Available online 2 November 2023

Edited by Jie Hao and Meng-Jiao Zhou

Keywords:
Electric submersible pump (ESP)
Entropy production theory
Energy characteristics
Inter-stage differences

ABSTRACT

The electric submersible pump (ESP) is a crucial apparatus utilized for lifting in the oil extraction process. Its lifting capacity is enhanced by the multi-stage tandem structure, but variations in energy characteristics and internal flow across stages are also introduced. In this study, the inter-stage variability of energy characteristics in ESP hydraulic systems is investigated through entropy production (EP) analysis, which incorporates numerical simulations and experimental validation. The EP theory facilitates the quantification of energy loss in each computational subdomain at all ESP stages, establishing a correlation between microscopic flow structure and energy dissipation within the system. Furthermore, the underlying causes of inter-stage variability in ESP hydraulic systems are examined, and the advantages and disadvantages of applying the EP theory in this context are evaluated. Consistent energy characteristics within the ESP, aligned with the distribution of internal flow structure, are provided by the EP theory, as demonstrated by our results. The EP theory also enables the quantitative analysis of internal flow losses and complements existing performance analysis methods to map the internal flow structure to hydraulic losses. Nonetheless, an inconsistency between the energy characterization based on EP theory and the traditional efficiency index when reflecting inter-stage differences is identified. This inconsistency arises from the exclusive focus of the EP theory on flow losses within the flow field, disregarding the quantification of external energy input to the flow field. This study provides a reference for the optimization of EP theory in rotating machinery while deeply investigating the energy dissipation characteristics of multistage hydraulic system, which has certain theoretical and practical significance.

1. Introduction

At present, there is an increasingly prominent global contradiction between energy supply and demand (Qiu et al., 2022). The electric submersible pump (ESP), which is extensively employed as a lifting device in oil extraction processes (Yang et al., 2021a,b), needs to be deployed deep into the oil layer with the tubing, and hence, is usually designed with multiple stages in series to meet the high head requirements (Takacs, 2017). However, the multi-stage configuration of the ESP enhances its lifting capacity and also leads to different inflow conditions between the stages, resulting in slight variations in performance and internal flow characteristics (Li et al., 2023). These differences accumulate with each stage added, significantly increasing the uncertainty in predicting the performance and energy characteristics of multi-stage ESPs. Consequently, investigating the mechanism of inter-stage interaction, mitigating unsteady flow in the internal flow field, and enhancing operational stability while reducing inter-stage variability have become hot research topics in the ESP system field.

With the advancement of flow theories, an increasing number of researchers are utilizing computational fluid dynamics (CFD)

* Corresponding author.
E-mail address: yangyang_ujs@outlook.com (Y. Yang).

https://doi.org/10.1016/j.petsci.2023.10.032

Nomenclature

D	outer diameter
E	local dissipation rate per unit mass
g	gravitational acceleration
H	head
k	turbulent kinetic energy
N	number of blades
n	rotation speed
n_s	specific speed
Q	flow rate
$\dot{Q}$	heat transfer rate
S	entropy
$\dot{S}_{\overline{D}}'''$	direct dissipation by mean velocity
$\dot{S}_{D'}'''$	direct dissipation by turbulent pulsation
$S_{\overline{D}}$	entropy production of direct dissipation
$S_{D'}$	entropy production of turbulent dissipation
S_T	total entropy production
S_W	entropy production of wall
t	time
T	temperature
T_0	absolute temperature
U_2	circumferential velocity
u_f	friction velocity
u_w	velocity vector of the near-wall region
V_{bb}	blade-to-blade velocity
$\dot{W}_{sh}$	shaft work
β	empirical coefficient
μ	dynamic viscosity
μ_t	turbulent viscosity
ρ	density
τ_w	wall shear stress
Φ	viscous dissipation function
ω	turbulent vortex frequency
d	diffuser
i	impeller
des	design
BEP	best efficiency point
CFD	computational fluid dynamics
ESP	electric submersible pump
EP	entropy production
EPR	entropy production rate
PS	pressure side
RANS	Reynolds average Navier-Stokes
SS	suction side
SST	shear-stress transport
VS	vortex stretching

techniques to analyze the hydraulic systems of ESPs. The use of CFD enables visualization of complex microscopic flow structures in ESP hydraulic systems, facilitating the development of understanding the flow characteristics and inter-stage variability in these systems. Stel et al. (2014) studied the impact of different viscosity media on the flow distribution and performance of ESP internal flow using CFD. The authors noted the variations in flow characteristics of the three-stage ESP hydraulic system and highlighted the significance of studying multi-stage arrangements while exploring ESP-related phenomena. Based on the previous study, Stel et al. (2015) conducted a comprehensive examination of multi-stage ESPs and summarized various numerical methods, validating their accuracy in predicting flow characteristics in ESPs. The findings emphasized the variation in flow characteristics at all stages of ESP hydraulic systems, highlighting the rationality and advantages of using a three-stage model for numerical calculations. Subsequently, Yang et al. (2021a,b) investigated the inter-stage differences in the flow field distribution and pressure pulsation characteristics in a typical three-stage ESP hydraulic system, employing experimental and numerical simulations. The study revealed that the dynamic and static interference between the impeller and diffuser in the chamber is the primary cause of pressure pulsation, and the corresponding pressure pulsation signal has inter-stage differences, reflecting the evident cascade phenomenon.

The reduction of energy loss in hydraulic machinery has been a longstanding area of interest as it has a significant impact on the efficiency and overall performance of the system. In the case of ESP hydraulic systems, efficiency not only reflects the performance of the system but also directly affects crude oil production rates. Hence, there is a pressing need for accurate prediction of energy loss in ESP hydraulic systems. The EP theory is originally applied to analyze the energy characteristics of turbomachinery. In the early 1990s, Denton (1990) provided a detailed description of the associated entropy generation in the internal flow field of turbomachinery, pointing out that entropy generation is the root cause of efficiency loss. In recent years, with the maturity of EP theory, as a new way to characterize energy loss, the EP method has been widely used in the evaluation of energy performance of rotating machinery (Chen et al., 2023). Different from the traditional analysis method of hydraulic losses, the EP method combines energy losses with the complex microscopic properties of the flow field inside the pump (Zhou et al., 2022), making it possible to quantify the energy losses. Hou et al. (2016) integrated EP theory with numerical simulations to analyze the internal flow and energy characteristics of a submersible pump. The study found that flow separation and backflow in rotating mechanical flow passages directly contributed to the increase in entropy production rate (EPR). Subsequently, Hou et al. (2017) analyzed the local EPR of each overflow component of the centrifugal pump and proposed a new system for evaluating energy loss in rotating machinery. Chang et al. (2019) used EP theory to investigate self-priming pumps and identified turbulent dissipation as the primary factor contributing to hydraulic losses in the system. Zhang et al. (2020) evaluated the energy loss of a side passage pump under different wrapping angles using the EP method based on CFD and obtained favorable results. Ji et al. (2020) employed the EP method to analyze the energy characteristics of the leakage vortex at the top of the impeller of a mixed-flow pump and accurately captured the microscopic energy loss distribution of the leakage vortex. Furthermore, Yu et al. (2022a, b) applied the entropy production theory to the hydraulic loss characterization of hydraulic turbine, and further considered the effect of cavitation phenomenon on the internal energy loss of hydraulic turbine while quantitatively evaluating the energy loss of the overflow components under different working conditions, leading to favorable outcomes. It is evident that the majority of existing studies concentrate on the application of EP in quantifying energy losses in hydraulic systems, highlighting its exceptional benefits in visualizing energy loss.

The inter-stage variation characteristics of multi-stage ESP have received some attention from scholars in related fields. However, the study remains incomplete as the energy loss characteristics and their distribution, caused by differences in internal flow field

distribution between the stages, have not been fully understood. Additionally, the coupling characteristics of hydraulic losses between the various stages of the multi-stage ESP hydraulic system have not yet been modeled, and there are still several limitations in the theory of inter-stage variability. The introduction of EP theory has offered novel ideas for analyzing the internal flow and energy characteristics of hydraulic machinery. Although previous research has demonstrated favorable results with the combination of EP theory and CFD in the analysis of corresponding rotating machinery, a thorough analysis of the advantages and disadvantages of applying EP analysis in multi-stage ESP hydraulic systems is still lacking.

The primary objective of this study is to analyze the inter-stage variability of multi-stage ESP by employing traditional methods and EP theory. The analysis is based on a combination of numerical simulations and experimental studies. Specifically, the research investigates the energy loss mechanisms at each stage of the ESP and quantifies the energy losses using EP theory. Furthermore, the study summarizes the coupling relationship between the microscopic flow structure and the distribution of energy losses in each stage of the multi-stage ESP. At the same time, the study points out the shortcomings of EP theory in quantifying energy dissipation in hydraulic systems. This study provides a comprehensive exploration of the energy dissipation characteristics in multistage hydraulic systems, also can offer guidance for optimizing EP theory in rotating machinery. The research holds certain theoretical and practical significance.

2. Models and numerical methods

2.1. Geometric models

In this paper, the model 250QJ80 ESP is selected as the object of study. Its basic design parameters are as follows: rated flow rate $Q = 80$ m^3/h, single-stage head $H = 20$ m, rated speed $n = 2850$ r/min, so its specific speed $n_s = 163.97$. The number of blades of the impeller $N_i = 6$; the number of vanes of the diffuser $N_d = 7$; the outer diameter D_i of the impeller and the outer diameter D_d of the diffuser are 151 mm and 180 mm respectively. The blades are spatially twisted to reduce hydraulic losses and improve the efficiency and cavitation resistance of the unit. Subsequently, a three-dimensional model is established based on Unigraphics NX 12.0, and the principal overflow components are represented, as depicted in Fig. 1. To obtain a comprehensive understanding of the differential unsteady flow structures occurring within each flow passage across each stage in the hydraulic system, a complete flow passage model of the three-stage ESP is utilized for numerical simulation, as illustrated in Fig. 2. The primary body of the single-stage computational domain is comprised of the impeller, space diffuser, and chamber, and the inlet and outlet extension pipes are positioned at the front and rear ends, correspondingly. To ensure complete turbulence development at the inlet and outlet and to augment the precision of the numerical computation, the length of the pipe is set to 10 times the impeller diameter.

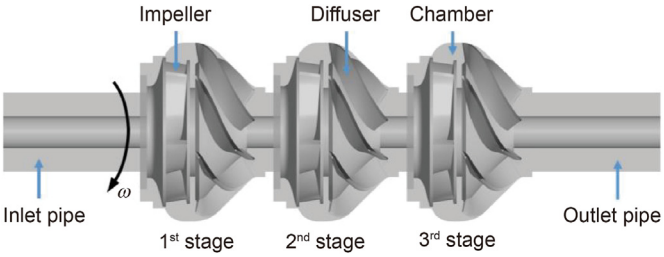

Fig. 2. Calculation domain of three-stage ESP.

Table 1
Number of grids for each case.

Case	1	2	3	4	5
Number of grids, 10^4	168	241	319	376	467

2.2. Grid and independence verification

The precision of numerical calculations is heavily influenced by the quantity, quality, and form of the computational grid. In contrast to unstructured grids, structured grids are more amenable to achieving congruent computational domain boundaries due to the orthogonal properties of their internal topology. Consequently, structured grids offer enhanced accuracy and robustness of the algorithm during computation. This study proposes the deployment of ANSYS TurboGrid for structured grid dissection of the computational subdomain of the three-stage ESP model, with a specific focus on ensuring grid quality in excess of 0.4 for both the impeller and diffuser.

Table 1 shows the detailed grid numbers of the five groups of grids used in the grid-independent analysis, and Fig. 3 shows the results of the model grid-independent analysis. The numerical simulation is based on the same control equations and boundary conditions, and the predicted values of head, efficiency and shaft power at $1.0Q_{des}$ operating conditions are chosen as the convergence parameters. It is not difficult to find that the numerical solutions of head, efficiency and shaft power gradually converge and the hydraulic performance of the ESP system gradually stabilizes when the number of grids increases to Case 3. Comparing the calculation results of Case 3 and Case 5, the predicted values of shaft power remain the same, while the average relative error of head and efficiency prediction is only 0.14%, which is less than 1%.

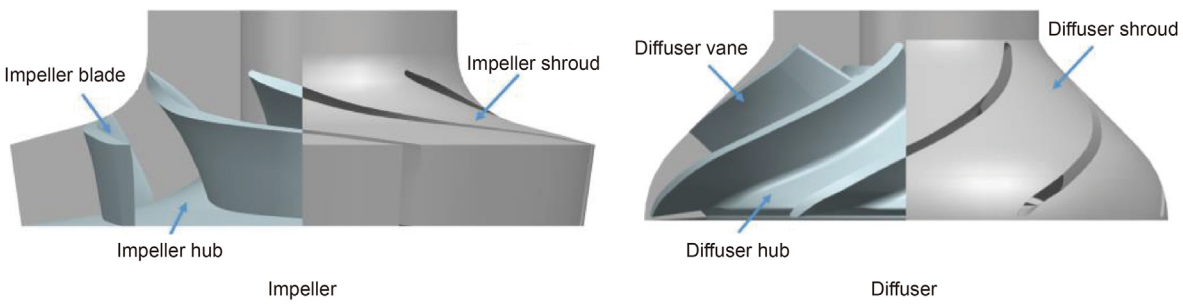

Fig. 1. 3D models of impeller and diffuser.

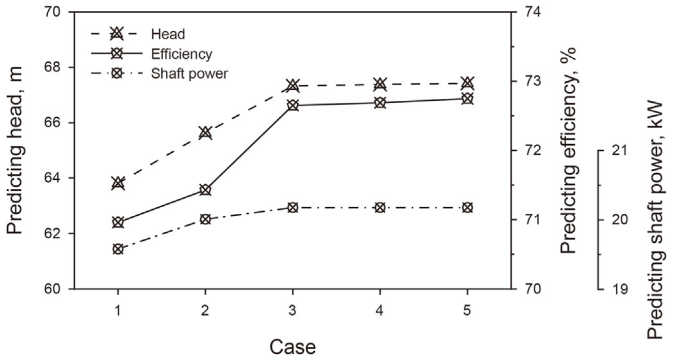

Fig. 3. Results of grid-independence analysis.

Therefore, we can assume that the accuracy of Case 3 meets the requirements. Considering the reasonable allocation of computational time and computational resources, the final grid number selected for the numerical calculation in this paper is 3.19 million, and the structured grid of the single passage of the impeller and diffuser is shown in Fig. 4.

2.3. Numerical calculation

Based on the shear-stress transport (SST) k-ω turbulence model, the full flow passage numerical simulation of the above multi-stage ESP system is performed using CFD software ANSYS CFX. The SST k-ω turbulence model modifies the definition of turbulent viscosity in the transport equation (Menter, 1994), and its turbulent viscosity μ_t is calculated as follows:

$$\mu_t = \rho \frac{a_1 k}{\max(a_1\omega, SF_2)} = \rho \min\left(\frac{k}{\omega}, \frac{a_1 k}{SF_2}\right) \tag{1}$$

$$F_2 = \tanh\left(\arg_2^2\right), \quad \arg_2 = \max\left(\frac{2\sqrt{k}}{0.09\omega y}, \frac{500v}{y^2\omega}\right) \tag{2}$$

$$S \equiv \sqrt{2S_{ij}S_{ij}} \tag{3}$$

$$S_{ij} = \frac{1}{2}\left(\frac{\partial u_j}{\partial x_i} + \frac{\partial u_i}{\partial x_j}\right) \tag{4}$$

where ρ is the density of the fluid medium; F_2 is the mixing function; S represents the strain rate magnitude; a_1 is the coefficient, and the default value is 0.31, which can be fine-tuned to correct the model, but the value cannot be reduced; y is the distance to the next surface; v is the kinematic viscosity of the fluid medium; S_{ij} represents the mean strain rate.

The above modified turbulent viscosity calculation takes into account the transmission of turbulent shear stress, which prevents over-prediction of turbulent viscosity during the calculation (Li et al., 2018) and is a better solution for turbulent effects in turbomachinery. The transport equations for its turbulent kinetic energy k and turbulent vortex viscosity frequency ω are as follows:

$$\frac{\partial}{\partial t}(\rho k) + \frac{\partial}{\partial x_i}(\rho k u_i) = \frac{\partial}{\partial x_j}\left(\Gamma_k \frac{\partial k}{\partial x_j}\right) + G_k - Y_k + S_k \tag{5}$$

$$\frac{\partial}{\partial t}(\rho \omega) + \frac{\partial}{\partial x_j}(\rho \omega u_j) = \frac{\partial}{\partial x_j}\left(\Gamma_\omega \frac{\partial \omega}{\partial x_j}\right) + G_\omega - Y_\omega + D_\omega + S_\omega \tag{6}$$

where t, ρ, G_k and G_ω denote the time term, fluid medium density, generation of turbulent kinetic energy and generation of turbulent dissipation rate, respectively; Γ_k and Y_k denote the effective diffusivity of k and dissipation under turbulence, respectively; Γ_ω and Y_ω denote the effective diffusivity of ω and dissipation under turbulence, respectively; D_ω denotes the cross-diffusion term; S_k and S_ω are the user-defined source terms.

It is known that in the dynamic process of medium flow, the near-wall normal direction has a large velocity gradient, which makes it difficult to predict the flow in the near-wall region during the numerical simulation. The analysis shows that the flow in the near-wall region can be subdivided into three layers (Schetz and Bowersox, 2011), namely, viscous sublayer, buffer layer and logarithmic layer, as shown in Fig. 5. In Fig. 5, u_τ and Δy represent the dimensionless velocity and wall normal distance of the flow layer, respectively. Among them, the viscous sublayer shows almost laminar flow due to the fluid viscosity. The outer logarithmic layer is dominated by turbulence, and the region between viscous sublayer and logarithmic layer is called buffer layer, where the fluid is affected by both viscous and turbulent effects with more complex flow characteristics. In this study, the wall function method is proposed to be used to solve the flow in the near-wall region. The wall function can model high-gradient shear layers near the wall with relatively coarse grids, without considering the viscous effects of the medium, thus saving a lot of CPU time and storage (Craft et al., 2004). In CFD, as the wall dimensionless distance, y^+ is

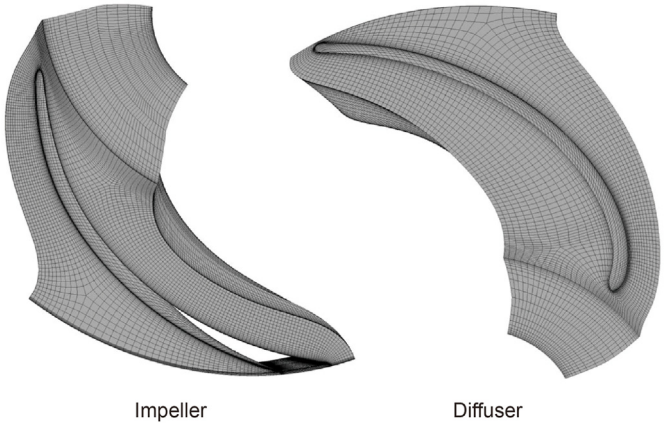

Fig. 4. Single passage grid of impeller and diffuser.

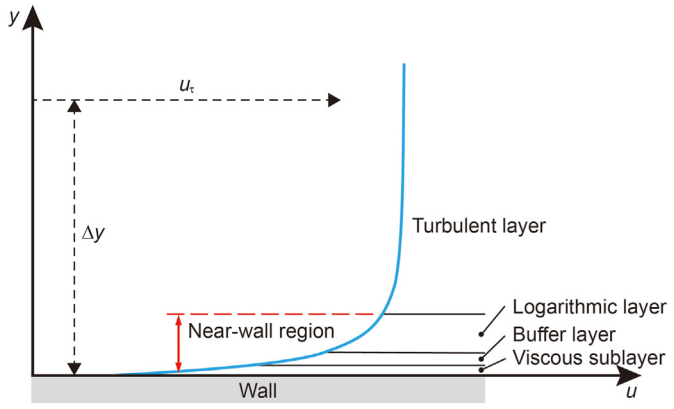

Fig. 5. Schematic diagram of the boundary layer.

often also used to characterize the thickness of the first grid layer at the boundary of the computational domain (Fuchs et al., 2012), which is calculated as

$$y^+ = \frac{yu_f}{\nu},\ u_f = \sqrt{\frac{\tau_w}{\rho}} \tag{7}$$

where, y is the distance to the wall; u_f is the friction velocity; ν is the kinematic viscosity of the medium; ρ is the density of the medium; τ_w is the wall shear stress.

It is worth noting that, as a low Reynolds number model, the ω-based turbulence model is very accurate in predicting the flow in the near-wall region. Nonetheless, this heightened accuracy comes at the cost of stringent boundary layer grid requirements, necessitating the proximity of y^+ value for the boundary layer grid to 1. Considering the trade-off between computational precision and cost, Automatic wall function in ANSYS CFX has supplanted the conventional near-wall treatment of low Reynolds number turbulence models. This transition effectively reduces the dependency of low Reynolds number models on high-quality boundary layer grids when simulating boundary layer flow. The adoption of the automatic wall function typically involves a specification that the first layer grid size maintains $30 < y^+ < 200$, ensuring all first layer grid nodes reside within the turbulent core region of the computational domain. Consequently, the boundary layer grid for the computational domain of the multi-stage ESP system has undergone meticulous refinement to secure numerical accuracy while satisfying the requirements for solving the automatic wall equations. The y^+ value in the near-wall region is maintained at an average of approximately 70, with upward and downward fluctuations restricted to no more than 20% across different flow conditions. Fig. 6 illustrates the distribution of y^+ values on the near-wall surface of the impeller and diffuser for the rated flow condition.

For the constant calculation, the inlet and outlet of the system are set as pressure inlet and mass outflow respectively, and the reference pressure is 1 atm. The stationary coordinate system is used for the extension pipes, all stages of the chamber and diffuser calculation subdomains, while the rotating coordinate system is used for the impeller calculation subdomains, and the speed is set to 2850 r/min. The wall is treated with no-slip boundary conditions, the roughness is set to 30 μm, and the near-wall boundary layer is treated with the standard wall function. Each subdomain is connected to each other through interfaces. In which, the sliding mesh method is used for data transfer between the rotating domain and the stationary domain, and the dynamic-static intersection interface is set as Frozen-Rotor, while the rest of the intersection interfaces are kept as general connection. To ensure the accuracy of the constant calculation, the residual target is set to 10^{-4} and the discrete format is set to second order.

3. Entropy production theory

The irreversible energy conversion processes in adiabatic systems are accompanied by the dissipation of energy (Ghorani et al., 2020). The dissipated energy that cannot be utilized is defined as the entropy of the system. The Gouy-Stodola theorem (Bejan, 2013) states that in the general case of unstable operation of open systems considering heat transfer, the first and second laws of thermodynamics prescribe that:

$$\frac{\partial E}{\partial t} = \sum_{in} \dot{m}\left(h + \frac{1}{2}V^2 + gz\right) - \sum_{out} \dot{m}\left(h + \frac{1}{2}V^2 + gz\right) + \dot{Q} - \dot{W}_{sh} \tag{8}$$

$$\frac{\partial S}{\partial t} \geq \sum_{in} \dot{m}s - \sum_{out} \dot{m}s + \frac{\dot{Q}}{T_0} \tag{9}$$

where E is local dissipation rate per unit mass; t is time; $\dot{m}$ is mass flow rate; h is heat transfer coefficient; V is speed; g is gravitational acceleration; z is longitudinal coordinate; $\dot{Q}$ is heat transfer rate; $\dot{W}_{sh}$ is shaft work; S is entropy; T_0 represents the absolute temperature of the environment.

In incompressible flow, where thermal entropy production is negligible (Liu et al., 2021), the EPR $\dot{S}_{pro}$ is proportional to the mechanical power $\dot{W}$ input to the hydraulic system from the prime mover:

$$\dot{S}_{pro} = \frac{\dot{W}}{T_0} \tag{10}$$

Then the EPR $\dot{S}'''_{pro}$ per unit time and unit volume in the system is

$$\dot{S}'''_{pro} = \frac{\dot{W}'''}{T} \tag{11}$$

where, $\dot{W}'''$ is the volumetric rate of mechanical power dissipated in volumetric micro elements by viscous shearing. At the same time, there is $\dot{W}'''$ equal to the product of the dynamic viscosity of the fluid medium and the viscous dissipation function Φ (Bird, 2002), hence:

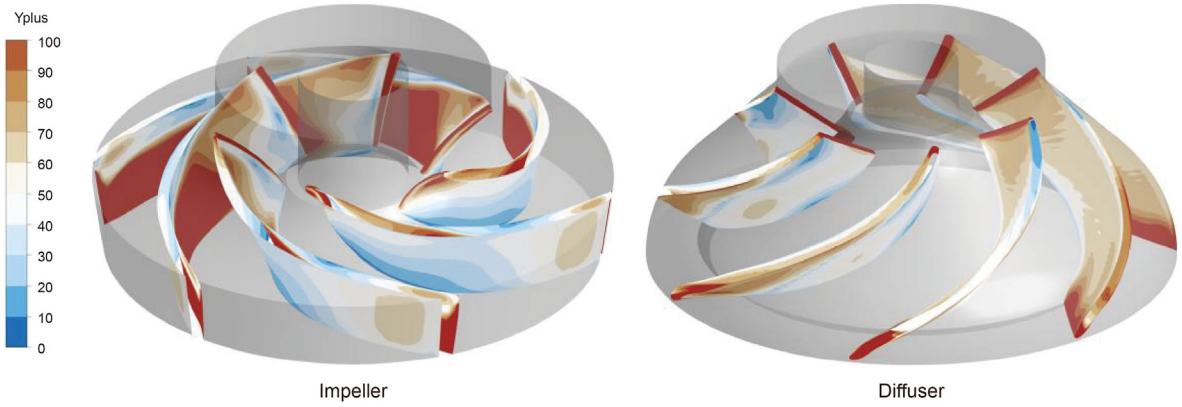

Fig. 6. y^+ distribution on the near-wall surface of the impeller and diffuser at $1.0Q_{des}$.

$$\dot{S}'''_{\mathrm{pro}} = \frac{\mu}{T}\Phi \tag{12}$$

Therefore, for an incompressible single-phase fluid medium, the total EPR $\dot{S}'''_{\mathrm{D}}$ per unit volume can be expressed as

$$\dot{S}'''_{\mathrm{D}} = \dot{S}'''_{\overline{\mathrm{D}}} + \dot{S}'''_{\mathrm{D}'} \tag{13}$$

$$\dot{S}'''_{\overline{\mathrm{D}}} = \frac{2\mu}{T}\left[\left(\frac{\partial \overline{u}_1}{\partial x_1}\right)^2 + \left(\frac{\partial \overline{u}_2}{\partial x_2}\right)^2 + \left(\frac{\partial \overline{u}_3}{\partial x_3}\right)^2\right] + \frac{\mu}{T}\left[\left(\frac{\partial \overline{u}_1}{\partial x_2} + \frac{\partial \overline{u}_2}{\partial x_1}\right)^2 + \left(\frac{\partial \overline{u}_1}{\partial x_3} + \frac{\partial \overline{u}_3}{\partial x_1}\right)^2 + \left(\frac{\partial \overline{u}_3}{\partial x_2} + \frac{\partial \overline{u}_3}{\partial x_2}\right)^2\right] \tag{14}$$

$$\dot{S}'''_{\mathrm{D}'} = \frac{2(\mu+\mu_{\mathrm{t}})}{T}\left[\left(\frac{\partial u'_1}{\partial x_1}\right)^2 + \left(\frac{\partial u'_2}{\partial x_2}\right)^2 + \left(\frac{\partial u'_3}{\partial x_3}\right)^2\right] + \frac{(\mu+\mu_{\mathrm{t}})}{T}\left[\left(\frac{\partial u'_1}{\partial x_2} + \frac{\partial u'_2}{\partial x_1}\right)^2 + \left(\frac{\partial u'_1}{\partial x_3} + \frac{\partial u'_3}{\partial x_1}\right)^2 + \left(\frac{\partial u'_3}{\partial x_2} + \frac{\partial u'_3}{\partial x_2}\right)^2\right] \tag{15}$$

where $\dot{S}'''_{\overline{\mathrm{D}}}$ denotes the direct dissipative EPR caused by the mean velocity, $\mathrm{kg\cdot m^{-1}\cdot s^{-3}\cdot K^{-1}}$; $\dot{S}'''_{\mathrm{D}'}$ denotes the turbulent dissipative EPR caused by the turbulent pulsation, $\mathrm{kg\cdot m^{-1}\cdot s^{-3}\cdot K^{-1}}$; $\overline{u}_1$, $\overline{u}_2$, $\overline{u}_3$ denote the components of the mean velocity in the x, y, z directions, m/s, respectively; u'_1, u'_2, u'_3 denote the components of the pulsation velocity in the x, y, z directions, m/s, respectively; T is the temperature of the adiabatic system, K; μ is the dynamic viscosity of the fluid medium, Pa·S, and μ_{t} is the turbulent dynamic viscosity of the fluid medium, Pa·S.

It is noteworthy that the Reynolds average Navier-Stokes (RANS) method adopted in this study solely furnishes average turbulence data and is unable to capture turbulent pulsations at every scale. Consequently, the turbulent dissipation EPR $\dot{S}'''_{\mathrm{D}'}$ due to the velocity component of fluid pulsation cannot be calculated. Nonetheless, Kock and Herwig (2004) provide an approximation algorithm for the EPR of turbulent dissipation in a RANS-based turbulence model:

$$\dot{S}'''_{\mathrm{D}'} = \beta\frac{\rho\omega k}{T} \tag{16}$$

where, β is the empirical coefficient, generally taken as 0.09; ρ is the fluid medium density, $\mathrm{kg\cdot m^{-3}}$; ω is the turbulent vortex viscous frequency, $\mathrm{s^{-1}}$; k represents the turbulent kinetic energy, $\mathrm{m^2\cdot s^{-2}}$.

At the meanwhile, the EPR has a strong wall effect. A study by Zhang et al. (2011) gives the calculation of the EP of the wall:

$$S_{\mathrm{W}} = \int_A \frac{\tau_{\mathrm{W}}\cdot u_{\mathrm{W}}}{T}\mathrm{d}A \tag{17}$$

where, τ_{W} is the wall shear stress, Pa; u_{W} is the velocity vector of the near-wall region, m/s; A is the surface area of the wall area subarea, $\mathrm{m^2}$.

Similar to the calculation of the wall EP, the direct and turbulent dissipative EP can be obtained by integrating the local EPR over the corresponding computational domain as follows:

$$S_{\overline{\mathrm{D}}} = \int_V \dot{S}'''_{\overline{\mathrm{D}}}\mathrm{d}V \tag{18}$$

$$S_{\mathrm{D}'} = \int_V \dot{S}'''_{\mathrm{D}'}\mathrm{d}V \tag{19}$$

where $S_{\overline{\mathrm{D}}}$ is the EP of direct dissipation, $\mathrm{kg\cdot m^2\cdot s^{-3}\cdot K^{-1}}$; $S_{\mathrm{D}'}$ is the EP of turbulent dissipation, $\mathrm{kg\cdot m^2\cdot s^{-3}\cdot K^{-1}}$; and V denotes the volume of the integration domain, $\mathrm{m^3}$. At this point, all three components of the total EP in the hydraulic system can be quantified, and the process of energy dissipation within the ESP hydraulic system is given in Fig. 7.

Hence, the total EP S_{T} of the system consists of the direct dissipative EP $S_{\overline{\mathrm{D}}}$, the turbulent dissipative EP $S_{\mathrm{D}'}$ and the wall EP S_{W}:

$$S_{\mathrm{T}} = S_{\overline{\mathrm{D}}} + S_{\mathrm{D}'} + S_{\mathrm{W}} \tag{20}$$

4. Experimental research

4.1. Test systems

Fig. 8 illustrates the schematic diagram of the ESP test system employed in this research. The torque meter utilized in this setup exhibits an accuracy grade of 0.25, whereas the rotational speed is measured with an accuracy grade of 0.1. Moreover, the pressure transmitter utilized in the test exhibits an accuracy grade of 0.25. The electromagnetic flow meter model is DN100, and the accuracy grade is 0.4. To guarantee test accuracy, the impeller and diffuser of the ESP are fabricated through precision casting of stainless steel.

In the experiment, ignoring the influence of the inlet and outlet velocity head, the measurement error E_{H} of the head is the measurement error of the pressure transmitter:

$$E_{\mathrm{H}} = \pm 0.25\% \tag{21}$$

The measurement error of the flow rate, E_{Q}, which is the error of the electromagnetic flow meter, has

$$E_{\mathrm{Q}} = \pm 0.40\% \tag{22}$$

The measurement error E_{T} of the shaft power is related to the measurement errors E_{N} and E_{M} of the rotational speed and torque:

$$E_{\mathrm{T}} = \sqrt{{E_{\mathrm{N}}}^2 + {E_{\mathrm{M}}}^2} = \pm 0.27\% \tag{23}$$

In summary, the total system error E_{S} of the ESP performance test system used in this study is

$$E_{\mathrm{S}} = \sqrt{{E_{\mathrm{H}}}^2 + {E_{\mathrm{Q}}}^2 + {E_{\mathrm{T}}}^2} = \pm 0.54\% \tag{24}$$

The analysis reveals that the cumulative error of the system falls well within the permissible range defined by the study, thereby ensuring the reliability and validity of the experimental data.

4.2. Experimental verification of hydraulic characteristics

The external characteristics of the relevant three-stage ESP are evaluated utilizing the aforementioned test system. The flow rate of the ESP system is regulated via electric valves, while the torque meter measures the output torque and speed of the motor. The pressure transmitter is utilized to measure the inlet and outlet pressure of the ESP system and subsequently convert it to head.

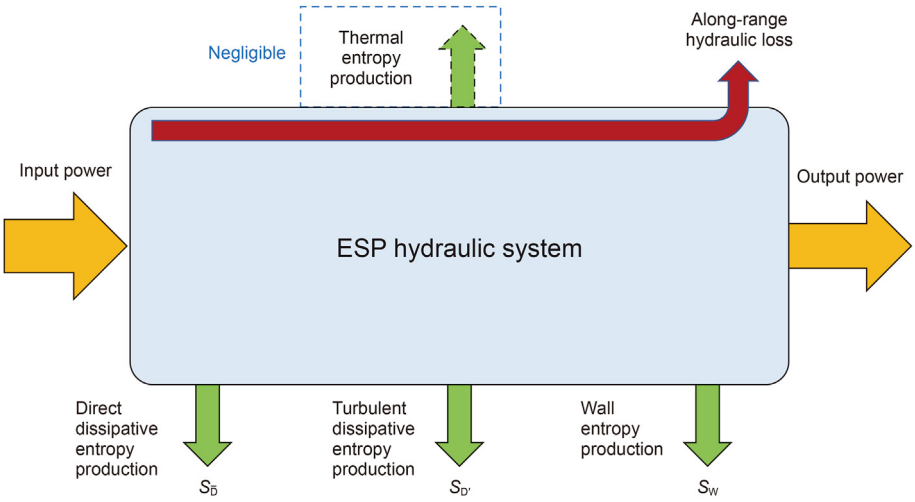

Fig. 7. Energy dissipation processes within the ESP hydraulic system.

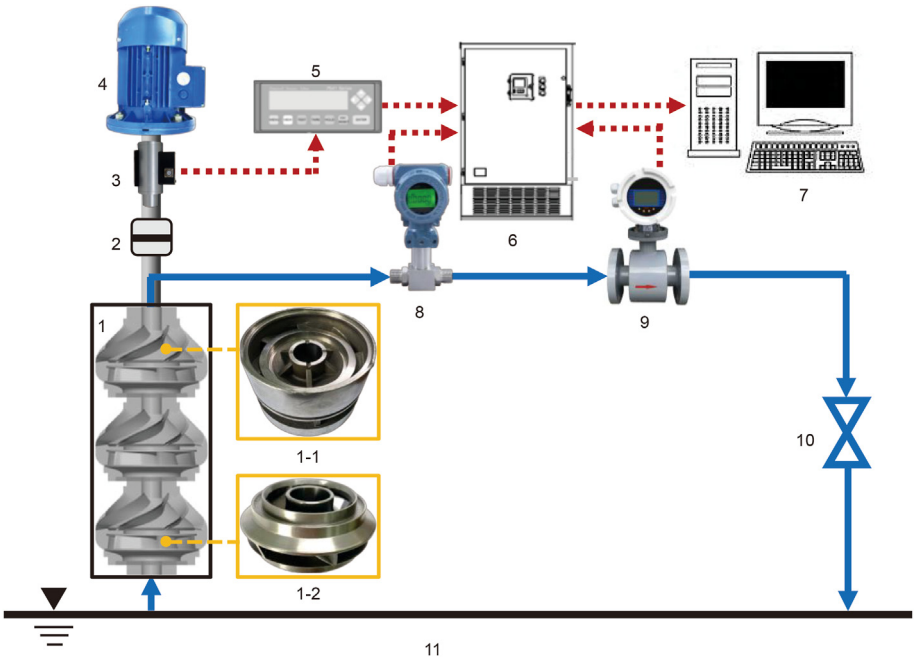

Fig. 8. Test system of ESP. Note: 1—three-stage ESP system; 1-1—stainless steel diffuser; 1-2—stainless steel impeller; 2— diaphragm coupling; 3—torque meter; 4—motor; 5—speed and torque synchronous collector; 6—test system control and data acquisition system; 7—computer; 8—pressure transmitter; 9—electromagnetic flow meter; 10—electric valve; 11— open pool.

Fig. 9 shows the comparison between the experimental and numerical simulation results of the external characteristics of ESP. As shown in Fig. 9, the experimental and simulated results of the three external characteristics parameters of the ESP follow the same trend in the full flow interval, and the experimental results of the shaft power and head are smaller than the numerical simulation predictions. When $Q < 0.5Q_{des}$, the prediction of shaft power is better, but the transient nature and uncertainty of the flow field are enhanced by the influence of stronger backflow and second flow and other undesirable flow patterns in the flow passage of ESP under low flow conditions, and the test results of head deviate more from the predicted results. When $Q > 0.5Q_{des}$, the test value of head and the predicted value change the same trend, and the average difference is stable at 4.1 m. However, there are large deviations between the experimental and predicted values of shaft power, and the amount of deviation is proportional to the magnitude of the flow rate. Notably, the highest agreement between the predicted and experimental results for device efficiency is observed, with only slightly lower predicted results occurring in the $1.0Q_{des}$–$1.5Q_{des}$ flow interval. In summarizing, the numerical method used in this paper accurately predicts the efficiency of the ESP hydraulic system, but there are still some deviations in the prediction of shaft power and head. Considering that the trends of the experimental and predicted results of the three external characteristics parameters all maintain a high degree of agreement, while integrating the experimental systematic errors and the uncertainties of the numerical simulations, the numerical method adopted in this study can be considered to have a high degree of accuracy.

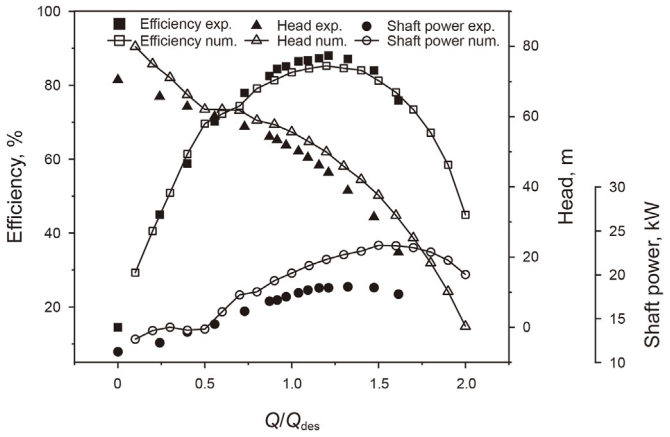

Fig. 9. Comparison between the experimental and numerical simulation results of the external characteristics of ESP.

5. Results and discussion

5.1. Intra-stage flow characteristics of multi-stage ESP

5.1.1. Internal flow characteristics of the impeller

Fig. 10 shows the distribution of the dimensionless velocity V_{bb}/U_2 at 0.5 Span section of the impeller at each stage for different flow conditions. Where V_{bb} denotes the component of blade-to-blade velocity and U_2 is defined as the circumferential velocity at the tip of the impeller blades. From Fig. 10, it can be seen that the flow rate of the medium in the impeller passage increases rapidly with the increase of the flow rate, but shows a different distribution pattern. When the ESP is operating at low flow rate ($0.6Q_{des}$), the axial flow velocity is small and the incoming flow angle is smaller than the blade inlet resting angle at the inlet due to the implication of the velocity. The smaller incoming flow angle allows the medium to collect on the pressure side (PS) of the blade when it enters the flow passage, causing flow separation on the SS of the blade. The low velocity zone formed by the flow separation phenomenon leads to a non-uniform distribution of pressure in the impeller passage, thus providing conditions for the generation of second flow. Meanwhile, the flow structure perpendicular to the main stream created by the second flow in the impeller passage makes the jet phenomenon of greater intensity appear at the outlet of the impeller under low flow conditions. As the flow rate increases, the axial velocity of the fluid medium at the inlet increases, and the incoming flow angle increases. The high-speed zone in the impeller passage is shifted to the suction side (SS) of the blade, and a small low speed zone is formed on the PS. In addition, it is easy to find that the velocity field distribution characteristics in the first impeller stage of ESP are obviously different from those in the last two impeller stages, while the velocity field distribution in the last two impeller stages has a high similarity. The main reason for this phenomenon is still the differential flow characteristics of the fluid medium at the inlet of the impeller. The incoming flow from the last two impeller stages is reduced by the rectification of the upper diffuser. However, the limited performance of the diffuser does not completely eliminate the residual circulation of the fluid medium, resulting in a change in the fluid flow angle of the fluid medium at the inlet of the second and third stage impellers. At the same time, the incoming flow angle has a large impact on the flow characteristics in the impeller passages, resulting in the second and third stage impellers showing a different velocity field distribution than

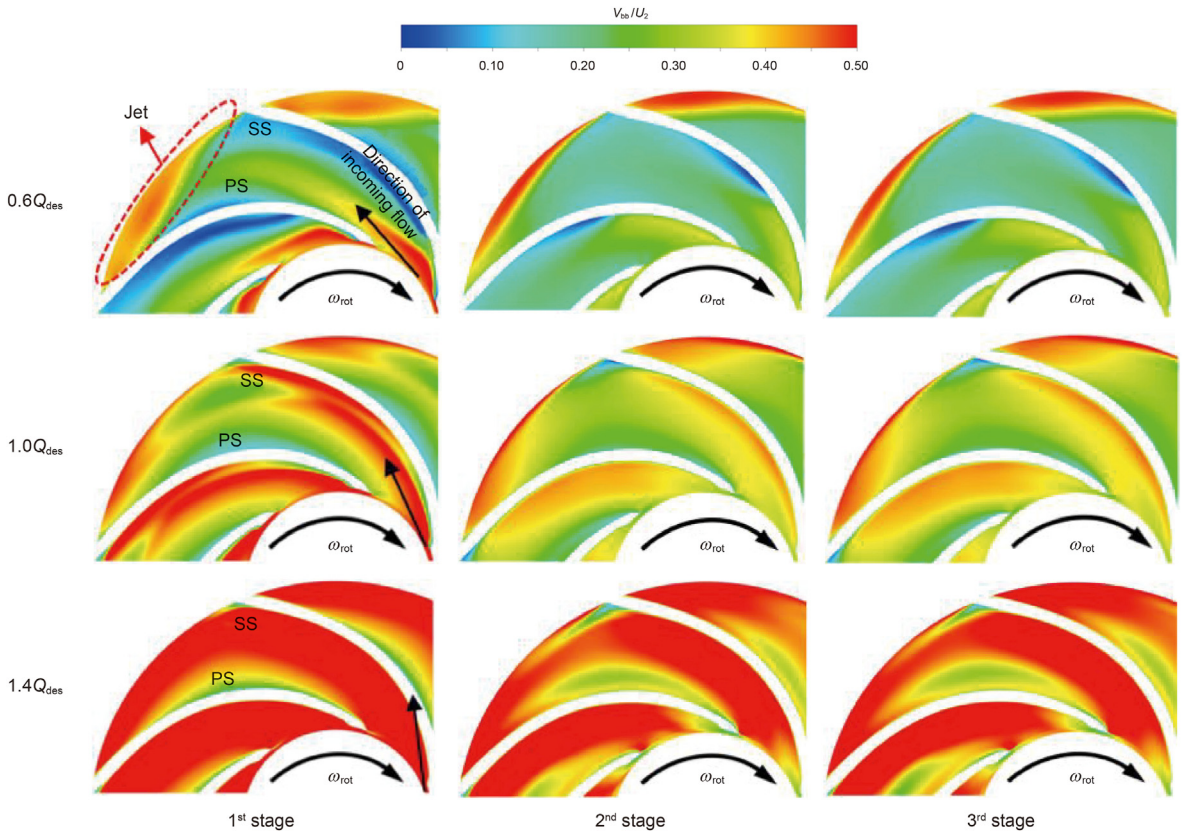

Fig. 10. Cross-sectional dimensionless velocity distribution at 0.5 Span of the impeller.

the first stage impeller.

5.1.2. Internal flow characteristics of the diffuser

The diffuser is placed below the impeller and is connected to the impeller through the pump chamber. In the pump device, the guide vane plays the role of deceleration and elimination of velocity circulation, etc., so as to convert the kinetic energy of the overflow medium into static pressure energy. The related research (Zhou et al., 2022) shows that the energy dissipation of the diffuser occupies the dominant position of the overall energy loss of the ESP under certain working conditions. It is of great significance to explore the distribution of EP in the diffuser to master the mechanism of energy loss in ESPs. In fluid mechanics, vortex stretching (VS) refers to the elongation of vortices in fluid flow and describes the core of the energy cascade of small and large scale vortices in turbulent flow (Buaria et al., 2020).

First consider the vorticity equation for the viscosity-free condition, expressed in Lagrangian form as

$$\frac{D\omega}{Dt} = \omega \cdot S, \quad S = \frac{\partial_\beta u_\alpha + \partial_\alpha u_\beta}{2} \tag{25}$$

where, $\omega \cdot S$ is the VS term. Since the strain rate tensor S is a symmetric second-order tensor, there is a characteristic decomposition:

$$S \equiv \lambda_\alpha e^{(\alpha)} \otimes e^{(\alpha)} \tag{26}$$

where, λ_α and $e^{(\alpha)}$ are the characteristic quantities of S and the corresponding eigenvectors. Thus, the VS term in turbulence can be characterized as

$$\omega \cdot S = \lambda_\alpha \omega \cdot \left(e^{(\alpha)} \otimes e^{(\alpha)} \right). \tag{27}$$

Meanwhile, Carbone and Bragg (2020) pointed out that VS helps to reduce the energy cascade while suppressing the dissipation rate of fluid kinetic energy. Fig. 11 shows the distribution of the VS intensity of the 0.5 Span section of the diffuser for different flow conditions. As can be seen from Fig. 11, the VS intensity in the diffuser increases with the flow rate, indicating that the VS intensity is related to the medium velocity. The high-speed fluid medium in the flow passage inhibits the development of the vortex system, thus hindering the energy exchange between the vortices, resulting in a reduction of the energy cascade in the flow passage. The associated vortex structure is elongated by the high-speed liquid flow medium, which is manifested as an increase in VS intensity. At the same time, it is not difficult to find that the distribution of high intensity VS regions is relatively independent of the flow conditions. The high-intensity VS region in the diffuser passage is mainly concentrated on the PS, and a certain range of low-VS region is formed on the SS. This phenomenon becomes more and more obvious with the increase of flow rate, and at high flow rate ($1.4Q_{des}$), the high VS intensity region occupies almost the whole flow passage. This is related to the unsteady flow characteristics of the incoming flow. In the small flow conditions, the medium at the inlet of the diffuser is accelerated by the rotating impeller and has a high velocity circulation, resulting in the incoming flow angle of the inlet of the diffuser is significantly larger than the blade inlet resting angle of the diffuser. At this time, the overflow capacity of the diffuser is much larger than the actual flow, causing a significant aggregation of the inlet medium at the PS of the blade due to

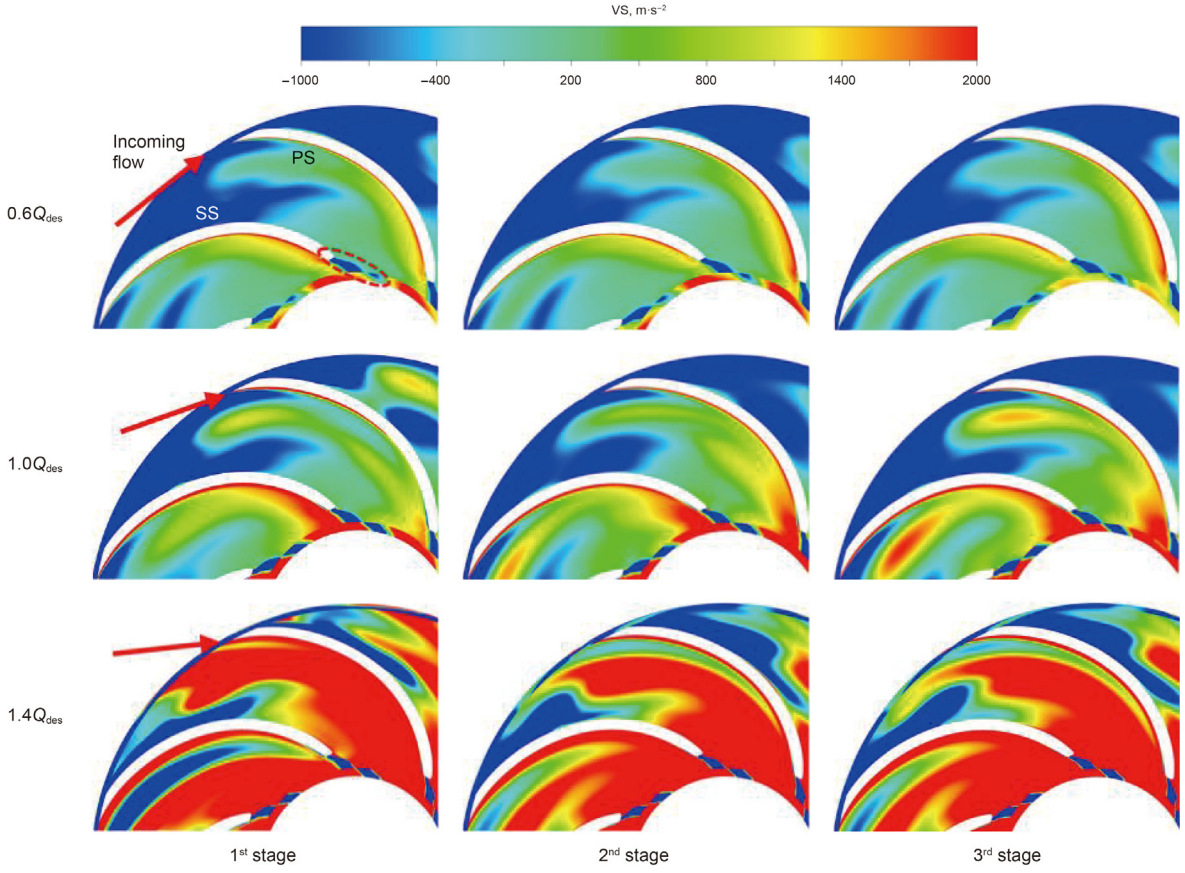

Fig. 11. VS intensity distribution in 0.5 Span section of diffuser.

the factors mentioned above. As the flow rate increases, the axial velocity of the fluid medium increases, and the incoming flow angle of the diffuser continues to increase, i.e., a larger area of high VS intensity is observed at high flow conditions. Comparing the VS distribution of the diffuser of each stage under different flow conditions, the VS distribution of the diffuser of each stage has high similarity with the inter-stage variability of the impeller. In addition, there is a periodically distributed region of low VS intensity at the outlet, which is the result of the residual velocity circulation of the fluid medium at the outlet interfering with the vanes of the diffuser.

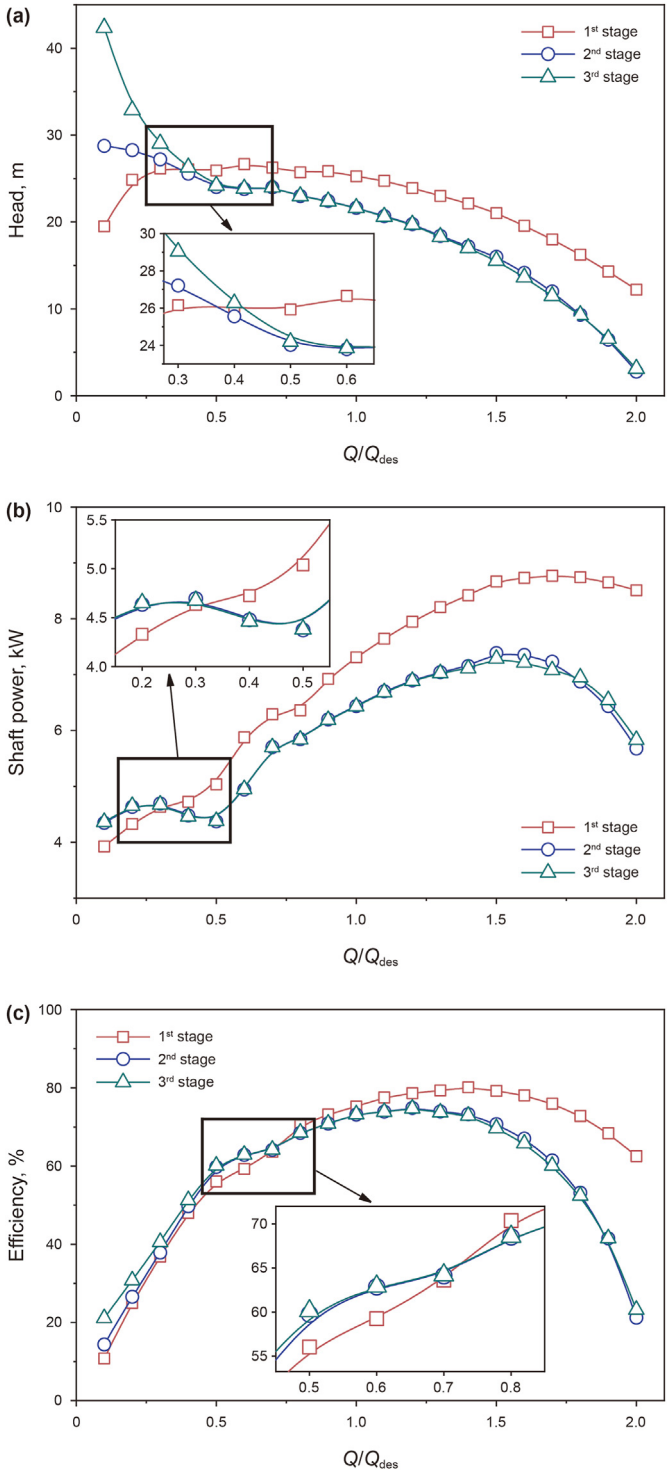

Fig. 12. Performance of ESP at all stages under different operating conditions. (a) Head; (b) shaft power; (c) efficiency.

5.2. Inter-stage characteristics of multi-stage ESP

5.2.1. Coupling characterization of performance and energy

Fig. 12 compares the performance of the ESP at all stages for full flow conditions. Overall, the performance of the three-stage ESP is highly correlated between the stages, but the performance of the second stage shows a high degree of consistency with that of the third stage. The underlying reason for this phenomenon is the difference in inflow conditions between the stages of the multi-stage ESP hydraulic system. As can be seen from Fig. 12(a), the head of each stage is basically the same under the $0.4Q_{des}$ flow condition, and as the flow rate decreases, the head of the second and third stages increases rapidly while the head of the first stage decreases significantly. When the flow rate is greater than $0.4Q_{des}$, the flow-head curves of the second and third stages overlap, and the head of the first stage exceeds that of the last two stages. At the same time, analysis of Fig. 12(b) shows that, as with the head, the variation of shaft power with flow at each stage shows the same strong inter-stage variability. The shaft power characteristics of the second and third stages remain highly consistent at full flow conditions. The shaft power of the first stage is smaller than that of the second and last stage when $Q < 0.3Q_{des}$, but increases rapidly with the flow and exceeds that of the second and last stage, and the difference is proportional to the flow. It is worth noting that the flow point for maximum power of the first stage is $1.7Q_{des}$, while the flow point for maximum power of the second and last stages is the same, both at $1.5Q_{des}$. In addition, observing Fig. 12(c), it is easy to find that when $Q < 0.7Q_{des}$, the ESP has the highest efficiency in the third stage, followed by the second stage, and the lowest efficiency in the first stage, which is related to the massive backflow at the inlet of the first-stage impeller under low flow conditions. The backflow at the inlet not only leads to energy dissipation, but also deteriorates the flow conditions in the first-stage impeller runner due to the large number of vortex clusters derived from the backflow, which directly leads to the low efficiency of the first stage of the ESP at low flow conditions. As the flow rate increases, the inlet conditions of the impeller of the first stage are greatly improved, while the residual velocity circulation of the inlet medium of the impeller of the last two stages becomes the main factor limiting the efficiency of the pump stage. Hence, it can be observed that as the flow rate increases, the efficiency of the first stage gradually exceeds that of the second and last stages and reaches the best efficiency point (BEP) at $1.4Q_{des}$, while the BEP of both the second and last stages is achieved at $1.2Q_{des}$.

Fig. 13 illustrates the distribution characteristics of the EP of the ESP system at full flow conditions. Analysing Fig. 13(a), it is easy to find that the distribution characteristics of the EP at each stage of the ESP system are highly consistent with the above conclusions on the external characteristics of ESP, i.e., the EP of the second and third stages of the three-stage ESP under different flow conditions is almost the same, while the EP of the first stage is somewhat different from the last two stages. Meanwhile, the lowest entropy-producing flow points of the first, second and last stages are located at $1.3Q_{des}$, $1.2Q_{des}$ and $1.1Q_{des}$, respectively. This indicates that there are still significant inter-stage variability and coupling in the energy dissipation characteristics of the flow field within the ESP. Under the full flow condition, the EP at all stages of ESP and the total EP show the characteristic of "U" shape distribution in general. When the flow rate is low, the EP decreases with increasing flow rate at all stages, but there are fluctuations in the flow rate range of

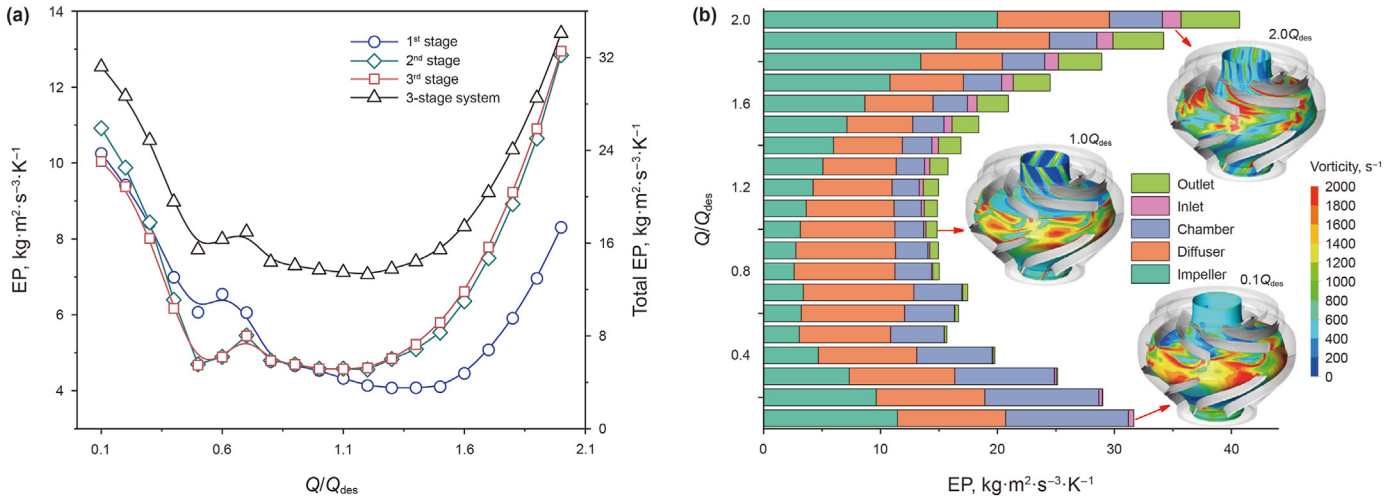

Fig. 13. Distribution characteristics of the EP in ESP at different flow conditions. (a) The EP of each stage of ESP and the total EP of the system; (b) EP stacking diagram with vorticity distribution at second stage.

$0.5Q_{des}$–$0.7Q_{des}$. The reason for this is mainly because the pump stalls in this flow interval, and a large amount of flow separation occurs on the SS of the impeller, resulting in a higher intensity backflow in the flow passage and a sharp increase in hydraulic losses. When the flow rate interval comes to $0.8Q_{des}$–$1.0Q_{des}$, the EP of the three stages of the ESP system is basically equal, indicating that the inter-stage energy difference characteristic of the 250QJ80 ESP is effectively curbed when the device is in the design condition, which ensures good stability during operation. In addition, the EP of the second and last stages gradually exceeds that of the first stage with the increase of the flow rate, and the increase is large. Nevertheless, it is essential to highlight that when comparing the efficiency (Fig. 12(c)) with the EP (Fig. 13(a)) for each stage of the three-stage ESP, an interesting observation emerges. While there is an overall trend of EP being inversely proportional to efficiency within each stage, there exist individual exceptions. For instance, at small flow conditions ($0.1Q_{des}$), the EP of the second stage of the system exhibits the highest value, while the first stage displays the lowest efficiency during this time. The presence of such anomalies can be attributed to the limitation of the existing EP theory, which solely accounts for energy losses within the flow field and does not consider the energy input from sources external to the hydraulic system. This highlights the need for a more comprehensive model that factors in external energy inputs to provide a more accurate representation of system behavior and performance.

As can be seen from Fig. 13(b), as the flow rate increases, the flow velocity inside the ESP system rises, while the turbulent dissipation and direct dissipation intensity at the outlet of the system increases due to the influence of the residual velocity circulation of the medium at the outlet of the diffuser, which is expressed as an entropy increase at the outlet of the system. The flow at the inlet of the system is not interfered by the complex flow inside the pump, and there is only a direct dissipative EP caused by the average velocity. Therefore, the EP is low, but still increases slowly with the increase of flow. It is worth mentioning that the statistics of the EP of the main overflow components all reflect a clear stall characteristic, which is consistent with the EP of the device. During the stall zone, the EP of the impeller and diffuser changes in characteristics opposite to the overall trend, which is rising. While the EP of the chamber continues to keep decreasing at this time, but the rate of decrease slows down. At low flow rates ($0.1Q_{des}$), the stability of the flow medium within the device experiences a marked decline, and the EP of the primary overflow components is considerably elevated. Owing to the "jet-wake" configuration, the high vorticity region within the impeller is predominantly concentrated at the outlet. Similarly, the high vorticity region in the pump chamber is regularly distributed near the outlet of the impeller passage. The high vorticity area in the diffuser is mainly concentrated in the PS of the leading edge. As the flow rate increases, the EP between the impeller and the chamber exhibits a significant decrease under rated flow rate conditions. Concomitant with the vorticity distribution of the second stage at this juncture, it can be ascertained that the high vorticity region within the impeller and chamber is markedly diminished, and the flow instability area caused by the "jet-wake" structure at the impeller outlet is likewise eliminated. This is related to the improvement of the inlet conditions of the system at rated flow conditions and the enhancement of the internal main-flow effect. As the flow rate continues to increase up to twice the rated flow rate, the inflow conditions of the impeller undergo a further deterioration. The incoming medium will impact the SS of the impeller blades directly, resulting in the formation of a large pressure gradient in the flow passage, and leading to an increase in flow separation and other unsteady flow structures. The aforementioned phenomenon results in a higher intensity of energy dissipation in the impeller passage, which is reflected in the surge of EP in the impeller. Simultaneously, the area of high vorticity inside the impeller also increases significantly, mainly distributed near the wall and SS of the blade. However, the inflow condition of the diffuser improves at this time, and the EP and vorticity inside are reduced.

5.2.2. Coupling analysis of flow and energy characteristics

Fig. 14 shows the distribution and flow field pattern of the dimensionless velocity V_{bb}/U_2 of the 0.5 Span cross-section for the three-stage ESP at the design condition. From Fig. 14, it can be seen that no significant unsteady flow phenomenon occurs in all stages of the impeller, but the incoming flow angle of the flow from the first stage impeller is significantly smaller than that of the second and third stage impellers. It has been pointed out above that this is caused by the residual velocity circulation of the incoming flow from the last two impeller stages. At the same time, a wide range of dynamic and static interference zones are observed in all stages of the pump chamber, i.e., the "jet-wake" phenomenon at the impeller outlet. The red high-speed area is the jet and the green low-speed

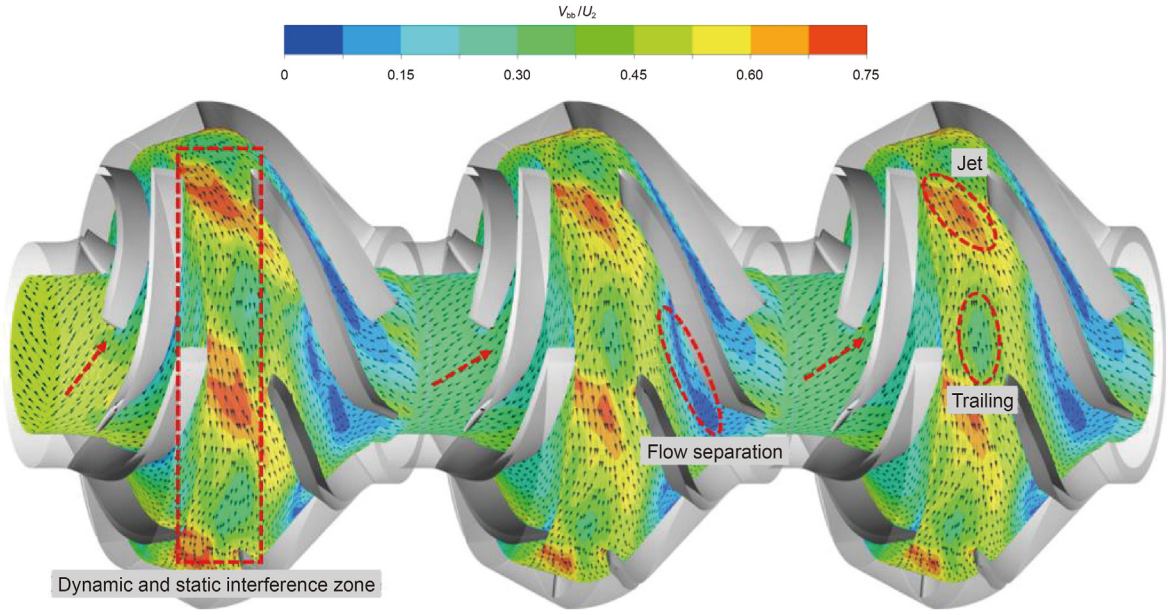

Fig. 14. Cross-sectional flow pattern of 0.5 Span for three-stage ESP at $1.0Q_{des}$.

area is the wake. It is not difficult to find that the pump chamber in the "jet-wake" intensity decreases stage by stage, and alternately along the circumference, which is related to the uneven distribution of media in the impeller. The incoming flow angle of the first stage impeller is small, resulting in a large number of fluid medium in the SS of the blade to gather, and the formation of high-intensity jet phenomenon at the outlet of the impeller. With the increase of incoming flow angle, the uneven distribution of fluid medium in the impeller is improved, and the jet intensity at the outlet of the last two impeller stages is weakened. In addition, there is a large range of flow separation in the diffuser flow passage at all stages, forming a low-speed vortex region, and its influence range is more stable and less related to the number of stages.

Fig. 15 shows the distribution of the EPR of the full flow passage of the three-stage ESP system at different flow conditions. As can be seen from Fig. 15, the overall EPR in the ESP flow passage gradually decreases with the increase of flow rate, and exhibits obvious inter-stage difference characteristics. A relatively high entropy region appears at the SS of the impeller inlet at low flow conditions ($0.6Q_{des}$) and radiates downstream along the impeller flow passage until it occupies the entire impeller. This is inseparable from the turbulent dissipation generated by the strong backflow and flow separation phenomenon at the impeller inlet. At the same time, it can be found that all stages of the chamber appear in the high entropy region of the periodical distribution, and the number of periods is equal to the number of impeller blades. This indicates that the "jet-wake" phenomenon at the impeller outlet caused by the static and dynamic interference effect is the direct cause of energy loss in the pump chamber. It is not difficult to find that the area of high entropy region in the first pump chamber is significantly higher than that in the last two chambers. Which is the result of the high intensity unsteady flow in the impeller flow passage propagating to the impeller outlet and coupling with the flow medium in the chamber. Immediately afterwards, the medium with strong turbulent pulsation characteristics in the chamber and the diffuser form potential flow and trailing interference, followed by the flow separation phenomenon in the flow passage of the diffuser, resulting in a higher intensity of turbulent dissipation between the top and SS of the diffuser, manifested as a high EPR in the corresponding region. Under the design flow condition ($1.0Q_{des}$), the flow pattern of the inlet medium of the first stage impeller is improved due to the increase in flow rate, and the high entropy-producing region in the impeller flow path disappears. The high entropy-producing region within the chamber and diffuser remains, but the intensity of energy loss is greatly reduced. In contrast, the overall EPR in the second and third chambers increased compared to the first stage. The limited performance of the diffuser does not completely eliminate the residual velocity circulation of the medium at the outlet of the diffuser. The velocity circulation of the medium couples with the axial velocity, leading to an increase in unstable flow structures in the second and third flow passages. More unsteady flow increases the intensity of dynamic and static interference in the chamber, bringing an increase in EPR, which is consistent with the inference above about the efficiency of multi-stage ESP at all stages. The EPR in the first-stage pump chamber remains at the lowest level under high flow conditions ($1.4Q_{des}$). However, as the overflow rate of the system approaches the maximum overflow capacity of the diffuser, the flow path of the diffuser is filled with the fluid medium. The space derived from the flow separation structure on the SS of the diffuser is squeezed, thus increasing the VS strength on the SS and suppressing the energy dissipation. However, the larger axial velocity interferes with the residual velocity circulation at the diffuser outlet, resulting in the flow angle of the inlet medium of the latter two stages being larger than the blade inlet resting angle of the impeller blades. The medium directly impacts the blade, which in turn forms a small area of high entropy on the PS at the inlet of the second and third impeller blades.

To further investigate the coupling between the flow mechanism and energy dissipation within the three-stage ESP, the EP distribution of the Blade to Blade section at Span = 0.9 for different flow conditions is given, as shown in Fig. 16. Under low flow conditions, significant backflow is observed at the inlet of the first stage impeller. When the flow rate is small, the incoming flow angle of the medium is smaller than the blade inlet resting angle of the impeller, causing strong impact at the tip of the blade. The fluid medium then flows back along the flow line near the wall from the inlet end of the impeller passage to the impeller inlet and into the

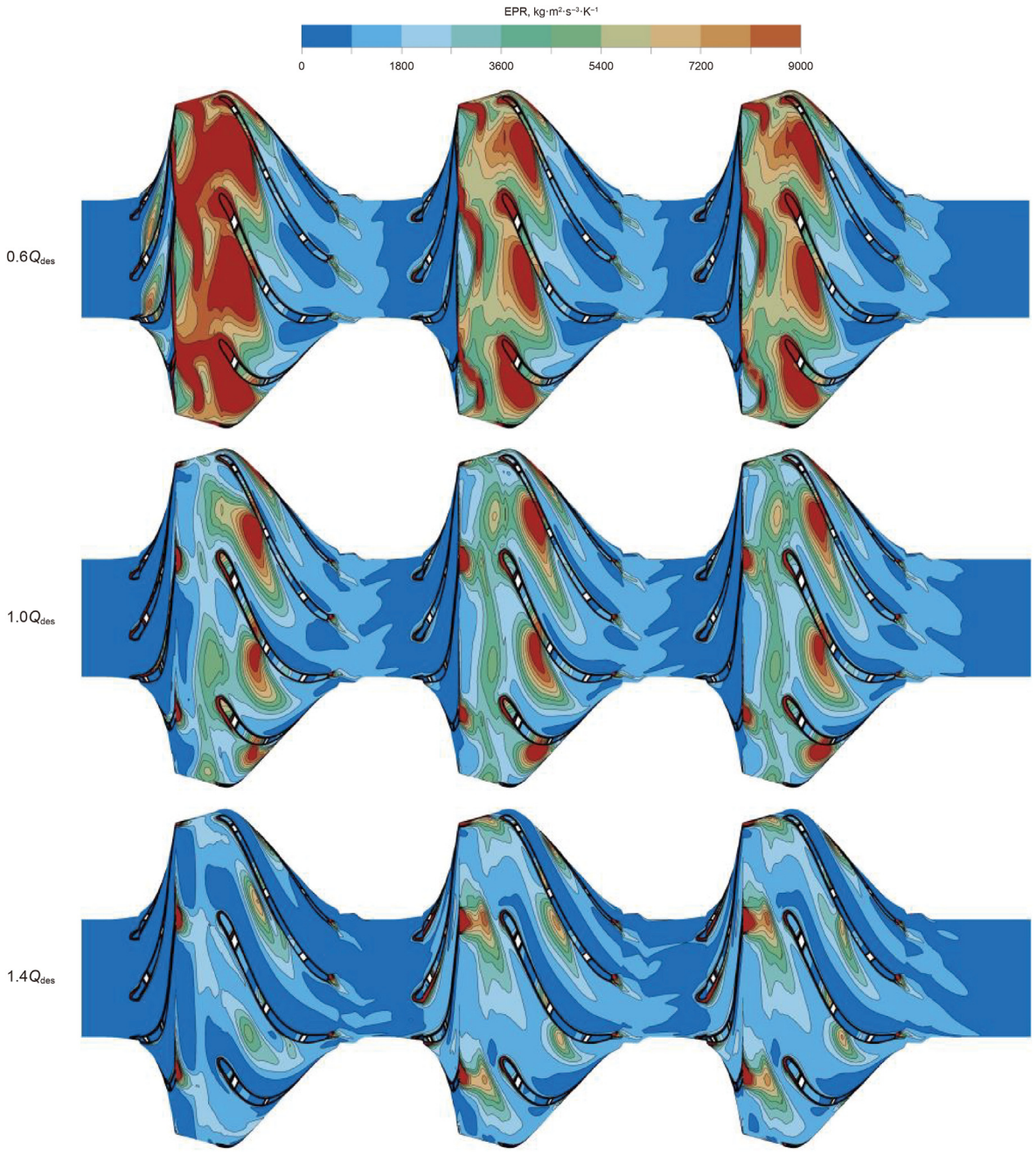

Fig. 15. Full-flow passage EPR distribution of ESP (Span = 0.5).

impeller inlet again. The extensive backflow action causes a dramatic deterioration of the impeller inflow pattern. A large number of backflow vortices in the flow passage to the inflow caused by the blocking effect, and the formation of dynamic and static interference at the first stage impeller inlet, increasing the energy dissipation of the corresponding fluid medium. Therefore, a high entropy region can be observed at the inlet of the first impeller stage under low flow conditions, which is distributed in strips and covers the blade inlet. However, as the inlet liquid flow angle increases in stages, the high EP region of the blade inlet gradually disappears. Small intensity flow separation exists on the SS of the impeller blade and a small area of energy dissipation is observed at the tip of the blade. Under the design conditions, the inflow pattern of the first stage impeller has been greatly improved, and the extensive reflux and high entropy areas have disappeared, but the flow separation caused by medium bias flow in the diffuser still exists. The flow separation forms a high pressure and low velocity zone. At the same time, due to the traction and stretching of the outer high-speed medium, resulting in higher vortex tensile strength in this region and lower dissipation rate of fluid kinetic energy. Upstream, the fluid is rapidly squeezed along the PS of the diffuser due to the deflecting effect. A higher velocity gradient and pressure gradient is formed, which increases the energy dissipation of the medium and creates a high entropy region within the diffuser flow path. At high flow conditions ($1.4Q_{des}$), the overflow of the diffuser increases, the flow pattern in the flow passage is better, and the flow separation phenomenon and the high entropy region both disappear. However, high entropy regions distributed along the

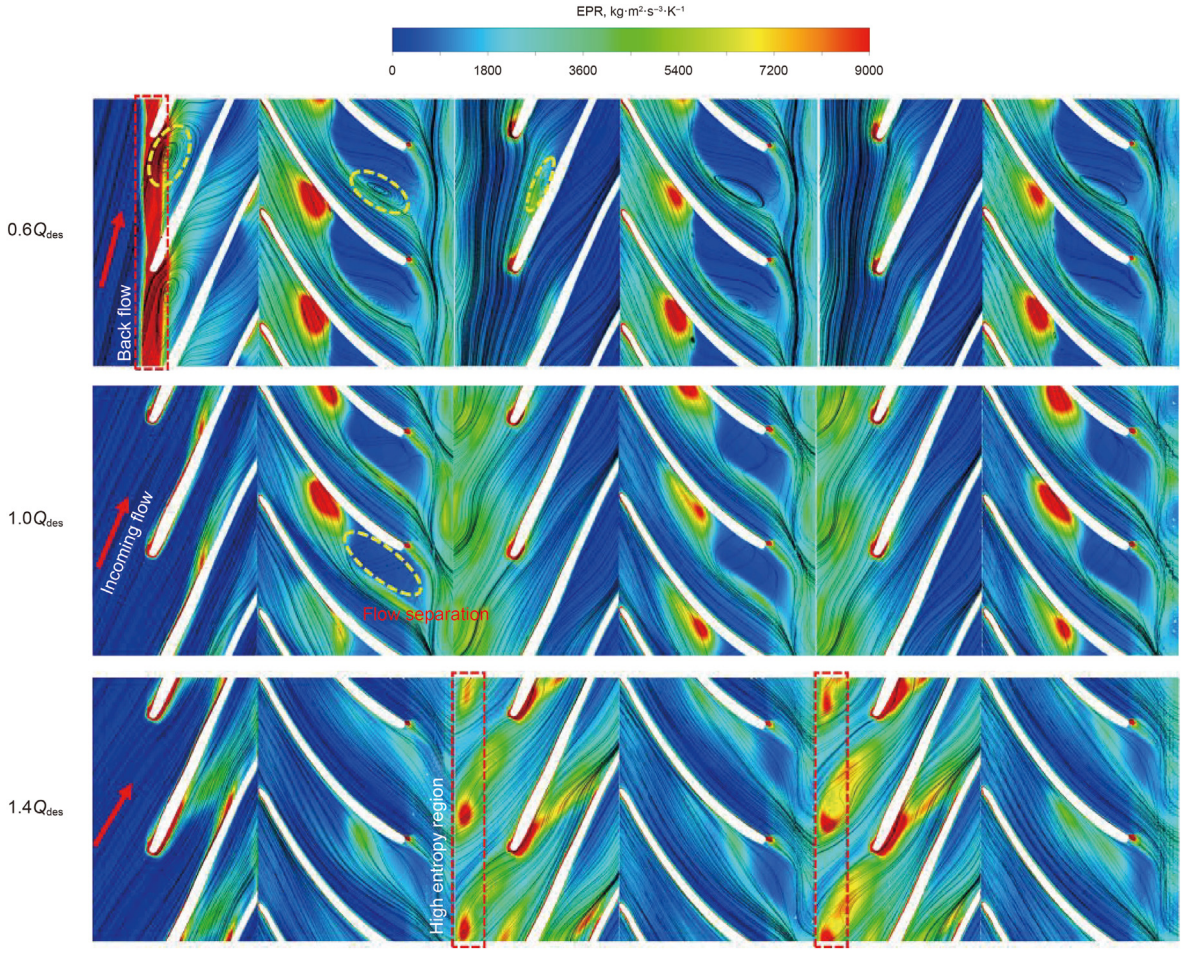

Fig. 16. Diagram of EPR of Blade to Blade section at Span = 0.9 under different flow conditions.

circumferential cycle are observed within the inlet of the second and third impellers, which are associated with unsteady flow within the impeller inlet. The high-speed medium on the PS of the diffuser forms a higher intensity turbulence in the inlet of the lower impeller after leaving the blade, which increases the turbulent dissipation in the corresponding area. This results in the formation of a high entropy region consistent with the number of blades of the diffuser, leading to a significantly lower efficiency of the hydraulic system of the second and third stages of the multi-stage ESP under high flow conditions.

6. Conclusion

This paper presents an in-depth analysis of the inter-stage performance and energy characteristics of multi-stage ESPs based on numerical simulations. Meanwhile, the energy loss of each stage is quantified using the EP theory. The coupling mechanism between the flow characteristics and energy loss at each stage of the multi-stage ESP is focused on, and the following conclusions are drawn:

(1) In the present investigation, a high level of agreement between the numerical and experimental results has been achieved, suggesting that the modeling and numerical methods, as well as the associated configurations utilized in this research, are rational, and the numerical computations are relatively precise. Moreover, the suitability of the SST k-ω model for addressing turbulence phenomena in rotating machinery has been validated.

(2) The utilization of EP theory in analysing the hydraulic system of the ESP has demonstrated consistency with the results of the flow field and performance analysis. The results show that the flow and energy characteristics of each pumping section in a three-stage ESP hydraulic system are highly correlated. However, the second and third stages have significantly higher similarity in their flow and energy characteristics compared to the first stage under the influence of inlet fluid pre-rotation. And the application of EP theory quantifies the energy loss while pinpointing the high energy loss region in the pump, which provides a new method to study the coupling characteristics of energy loss and flow structure of ESP.

(3) Although the EP theory has advantages over the traditional pump performance evaluation system, it does not combine the energy loss of the hydraulic system with the system efficiency. At the same time, the inconsistency between the energy characteristic analysis based on EP theory and the traditional efficiency index in the reflection of inter-stage differences is the result of the existing EP theory reflecting only the flow loss within the flow field without considering the energy input outside the flow field. Hence, the EP analysis method can only be used as an auxiliary means of the traditional hydraulic performance analysis method, and cannot build an independent performance evaluation system

based on the traditional EP theory, which has certain shortcomings.

To sum up, CFD-based EP analysis proves to be an effective tool for visualizing and quantifying local and overall losses in hydronic systems. Engineers can leverage CFD in the pre-design and prototype testing phases to determine the overall performance of the system and identify regions with high energy losses in the hydrodynamic model. This information, along with traditional performance calibration methods and EP theory as a supplementary tool, enables engineers to guide the geometric and spatial design of the hydraulic model for optimizing the corresponding performance of hydraulic machinery and reducing energy consumption. Nevertheless, the existing theory falls short in achieving an integrated understanding of energy dissipation and system (or local) efficiency in hydraulic machinery. The system efficiency can only be determined using the conventional pressure drop method. In the context of the multistage hydraulic system discussed in this paper, a large entropy production in its flow field does not necessarily indicate low efficiency. Thus, further optimization of EP theory is required to address these limitations effectively. In future studies, it would be beneficial to consider quantifying the total energy input to the hydraulic system from external sources in addition to capturing energy dissipation using the traditional EP theory. This can help optimize the relevant energy theory and address the shortcomings of the current EP theory.

Declaration of competing interest

The authors declare that they have no known competing financial interests or personal relationships that could have appeared to influence the work reported in this paper.

Acknowledgment

This research was financially supported by the China Postdoctoral Science Foundation (Grant No. 2023M732979 and No. 2022TQ0127), the Cooperative Research Project of the Ministry of Education's "Chunhui Program" (Grant No. HZKY20220117) the Natural Science Foundation of Jiangsu Province (Grant No. BK20220587), and the National Natural Science Foundation of China (Grant No. 52309112).

References

Bejan, A., 2013. Entropy generation minimization: the method of thermodynamic optimization of finite-size systems and finite-time processes. CRC press. https://doi.org/10.1201/9781482239171.

Bird, R.B., 2002. Transport phenomena. Appl. Mech. Rev. 55 (1), R1–R4. https://doi.org/10.1115/1.1424298.

Buaria, D., Bodenschatz, E., Pumir, A., 2020. Vortex stretching and enstrophy production in high Reynolds number turbulence. Physical Review Fluids 5 (10), 104602. https://doi.org/10.1103/PhysRevFluids.5.104602.

Carbone, M., Bragg, A.D., 2020. Is vortex stretching the main cause of the turbulent energy cascade? J. Fluid Mech. 883, R2. https://doi.org/10.1017/jfm.2019.923.

Chang, H., Shi, W., Li, W., et al., 2019. Energy loss analysis of novel self-priming pump based on the entropy production theory. J. Therm. Sci. 28 (2), 306–318. https://doi.org/10.1007/s11630-018-1057-5.

Chen, Z., Yang, S., Li, X., et al., 2023. Investigation on leakage vortex cavitation and corresponding enstrophy characteristics in a liquid nitrogen inducer. Cryogenics 129, 103606. https://doi.org/10.1016/j.cryogenics.2022.103606.

Craft, T.J., Gant, S.E., Iacovides, H., et al., 2004. A new wall function strategy for complex turbulent flows. Numer. Heat Tran., Part B: Fundamentals 45 (4), 301–318. https://doi.org/10.1080/10407790490277931.

Denton, J.D., 1990. Entropy generation in turbomachinery flows. SAE Trans. 99, 2251–2263. https://doi.org/10.4271/902011.

Fuchs, M., Waidmann, W., Macdonald, M., 2012. CFD simulation and grid study of a cavitating orifice flow. Int. J. Fluid Mech. Res. 39 (2), 160–169. https://doi.org/10.1615/InterJFluidMechRes.v39.i2.60.

Ghorani, M.M., Haghighi, M.H.S., Maleki, A., et al., 2020. A numerical study on mechanisms of energy dissipation in a pump as turbine (PAT) using entropy generation theory. Renew. Energy 162, 1036–1053. https://doi.org/10.1016/j.renene.2020.08.102.

Hou, H., Zhang, Y., Li, Z., 2017. A numerically research on energy loss evaluation in a centrifugal pump system based on local entropy production method. Therm. Sci. 21 (3), 1287–1299. https://doi.org/10.2298/TSCI150702143H.

Hou, H., Zhang, Y., Li, Z., et al., 2016. Numerical analysis of entropy production on a LNG cryogenic submerged pump. J. Nat. Gas Sci. Eng. 36, 87–96. https://doi.org/10.1016/j.jngse.2016.10.017.

Ji, L., Li, W., Shi, W., et al., 2020. Energy characteristics of mixed-flow pump under different tip clearances based on entropy production analysis. Energy 199, 117447. https://doi.org/10.1016/j.energy.2020.117447.

Kock, F., Herwig, H., 2004. Local entropy production in turbulent shear flows: a high-Reynolds number model with wall functions. Int. J. Heat Mass Tran. 47 (10–11), 2205–2215. https://doi.org/10.1016/j.ijheatmasstransfer.2003.11.025.

Li, T., Hemida, H., Zhang, J., et al., 2018. Comparisons of shear stress transport and detached eddy simulations of the flow around trains. J. Fluid Eng. 140 (11), 111108. https://doi.org/10.1115/1.4040672.

Li, X., Ouyang, T., Lin, Y., et al., 2023. Interstage difference and deterministic decomposition of internal unsteady flow in a five-stage centrifugal pump as turbine. Phys. Fluids 35 (4). https://doi.org/10.1063/5.0150300.

Liu, Y., Li, X., Lin, Z., et al., 2021. Numerical analysis of thermo-sensitive cavitating flows with special emphasises on flow separation and enstrophy conversion. Int. Commun. Heat Mass Tran. 125, 105336. https://doi.org/10.1016/j.icheatmasstransfer.2021.105336.

Menter, F.R., 1994. Two-equation eddy-viscosity turbulence models for engineering applications. AIAA J. 32 (8), 1598–1605. https://doi.org/10.2514/3.12149.

Qiu, R., Liang, Y., Liao, Q., et al., 2022. Primary logistics planning of oil products under the imbalance of supply and demand. Petrol. Sci. 19 (4), 1915–1925. https://doi.org/10.1016/j.petsci.2022.03.021.

Schetz, J.A., Bowersox, R.D., 2011. Boundary Layer Analysis. American Institute of Aeronautics and Astronautics. https://doi.org/10.2514/4.868245.

Stel, H., Sirino, T., Ponce, F.J., et al., 2015. Numerical investigation of the flow in a multistage electric submersible pump. J. Petrol. Sci. Eng. 136, 41–54. https://doi.org/10.1016/j.petrol.2015.10.038.

Stel, H., Sirino, T., Prohmann, P.R., et al., 2014. CFD investigation of the effect of viscosity on a three-stage electric submersible pump. In: Fluids Engineering Division Summer Meeting. American Society of Mechanical Engineers, FEDSM2014-21538. https://doi.org/10.1115/FEDSM2014-21538

Takacs, G., 2017. Electrical submersible pumps manual: Design, operations, and maintenance. Gulf professional publishing. https://doi.org/10.1016/C2017-0-01308-3.

Yang, Y., Zhou, L., Hang, J., et al., 2021a. Energy characteristics and optimal design of diffuser meridian in an electrical submersible pump. Renew. Energy 167, 718–727. https://doi.org/10.1016/j.renene.2020.11.143.

Yang, Y., Zhou, L., Shi, W., et al., 2021b. Interstage difference of pressure pulsation in a three-stage electrical submersible pump. J. Petrol. Sci. Eng. 196, 107653. https://doi.org/10.1016/j.petrol.2020.107653.

Yu, A., Li, L., Ji, J., et al., 2022a. Numerical study on the energy evaluation characteristics in a pump turbine based on the thermodynamic entropy theory. Renew. Energy 195, 766–779. https://doi.org/10.1016/j.renene.2022.06.077.

Yu, A., Tang, Y., Tang, Q., et al., 2022b. Energy analysis of Francis turbine for various mass flow rate conditions based on entropy production theory. Renew. Energy 183, 447–458. https://doi.org/10.1016/j.renene.2021.10.094.

Zhang, F., Appiah, D., Hong, F., et al., 2020. Energy loss evaluation in a side passage pump under different wrapping angles using entropy production method. Int. Commun. Heat Mass Tran. 113, 104526. https://doi.org/10.1016/j.icheatmasstransfer.2020.104526.

Zhang, X., Wang, Y., Xu, X., et al., 2011. Energy conversion characteristic within impeller of low specific speed centrifugal pump. Trans. Chin. Soc. Agric. Mach. 42 (7), 75–81. https://doi.org/10.3969/j.issn.1000-1298.2011.07.015 (in Chinese).

Zhou, L., Hang, J., Bai, L., et al., 2022. Application of entropy production theory for energy losses and other investigation in pumps and turbines: A review. Appl. Energy 318, 119211. https://doi.org/10.1016/j.apenergy.2022.119211.